7

Shock-Induced Turbulent Boundary Layer Separation in Over-Expanded Rocket Nozzles: Physics, Models, Random Side Loads, and the Diffusive Character of Stochastic Rocket Ascent

R. G. Keanini, T. D. Nortey, Karen Thorsett-Hill, N. Srivastava,
Sam Hellman, P. T. Tkacik and P. Douglas Knight
Department of Mechanical Engineering & Engineering Science
The University of North Carolina at Charlotte
USA

1. Introduction

Contrary to popular belief, and notwithstanding two hundred years of scientific study (Gruntman , 2004), the problem of accurately predicting rocket ascent remains largely unsolved. The difficulties trace to a variety of altitude-, speed-, and launch-site-dependent random forces that act during rocket ascent, including: i) aerodynamic forces (Sutton & Biblarz, 2001), ii) forces due to wind and atmospheric turbulence (Flemming et al., 1988; Justus & Johnson, 1999; Justus et al., 1990; Leahy, 2006), iii) forces produced by rocket construction imperfections (Schmucker, 1984), and iv) impacts with air-borne animals and debris (McNaughtan, 1964). Significantly, our physical understanding and ability to model the dynamical effects of each of these random features is fairly well-developed.

By contrast, understanding of the *physical origins,* as well as the *dynamical effects* of altitude-dependent, in-nozzle *random side loads,* has only recently begun to emerge (Keanini et al., 2011; Ostlund, 2002; Srivastava et al., 2010). Referring to figures 1 through 3, we find that side loads represent the end result of a chain of in-nozzle fluid dynamic processes. During low altitude flight, under over-expanded flight conditions, a pressure gradient can exist between the high pressure ambient air surrounding the rocket and nozzle, and the low pressures extant within the nozzle. This pressure gradient can force ambient air *upstream* along the nozzle wall; eventually, inertia of the ambient inflow is overcome by the pressure and inertial forces associated with the outflow, producing a near-wall recirculation region. To the supersonic flow outside the near-wall boundary layer, the recirculation zone functions as a virtual compression corner, producing an oblique shock (Keanini & Brown, 2007; Ostlund, 2002; Summerfield et al., 1954). See figures 1 through 3. Due to the altitude dependence of $P_a = P_a(H(t))$, where P_a is the ambient pressure and $H(t)$ is the rocket's time-dependent altitude, the nominal location of the oblique shock, $x_{shock} = x_{shock}(H(t))$, also varies with altitude.

Random side loads arise due to two coupled flow features: i) The oblique shock produces a sharp, adverse pressure rise within the near-wall outflow boundary layer, forcing the boundary layer to separate from the nozzle wall; see figure 1. ii) The *shape* of the boundary

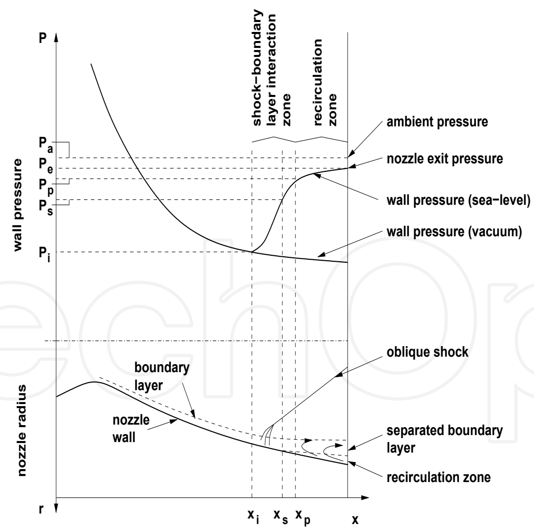

Fig. 1. Schematic of shock-induced boundary layer separation in rocket nozzles. The pressure variation shown is characteristic of free interaction separation problems. Adapted from Ostlund (2002).

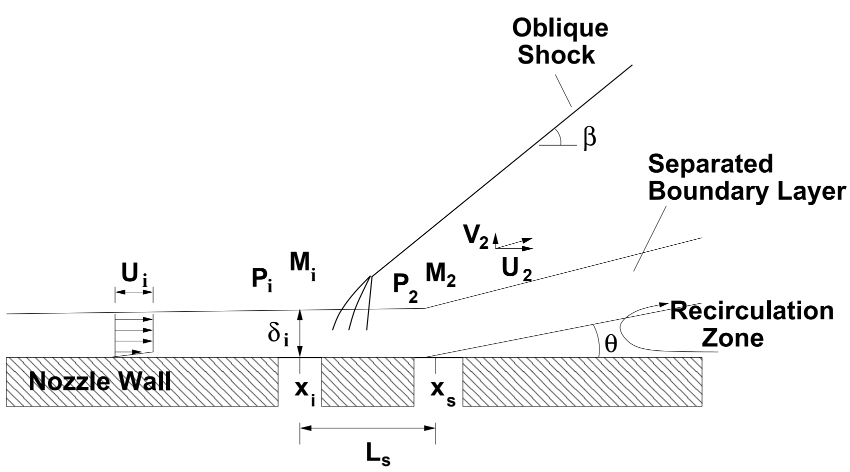

Fig. 2. Shock-induced boundary layer separation in overexpanded supersonic nozzle flow. The process typically occurs during low altitude flight when ambient pressure is high enough to force atmospheric air into the nozzle. The incoming air flows upstream along the low-inertia, near-wall region until downstream-directed boundary layer inertia turns it, forming a virtual compression corner. An oblique shock thus forms, and the combined action of shock-induced pressure rise and inertial pressurization produced by the inflow forces the down-flow boundary layer to separate. Pressures, mach numbers, and velocities are denoted, respectively, by P, M, and U and V. Axial positions where the boundary layer starts to thicken (i denotes *incipient*), and where it separates are denoted, respectively, as x_i and x_s; the nominal shock-boundary layer interaction zone is shown as L_s. Since the separation line position, x_s, and downstream conditions vary with the altitude-dependent ambient pressure, $P_a = P_a(H(t))$ (Keanini & Brown, 2007), all variables shown likewise vary with $H(t)$.

layer separation line, which at any instant, forms a closed curve along the nozzle periphery, varies randomly in space and time; see figure 3. Due to relatively uniform pressure distributions extant on the up- and downstream sides of the instantaneous separation line

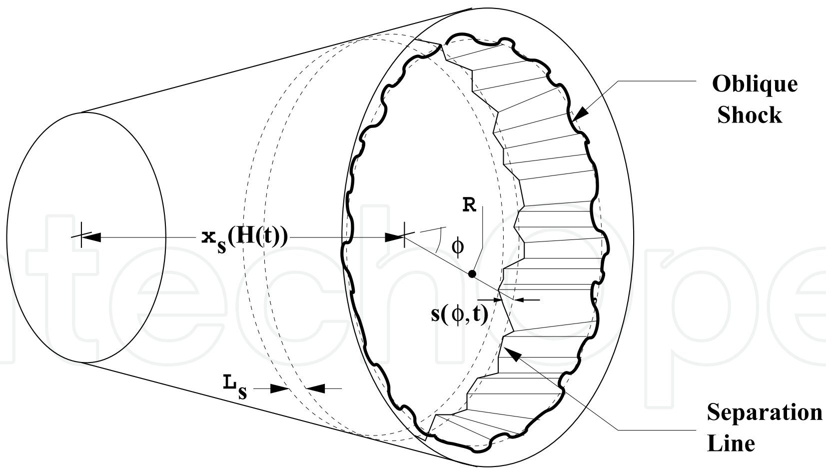

Fig. 3. Schematic of stochastic boundary layer separation line and associated, rippled, azimuthal oblique shock. The mean separation line position relative to the nozzle throat, x_s, varies with rocket altitude, $H(t)$; the corresponding nozzle radius is $R = R(H(t))$. The instantaneous separation line position relative to $x_s(t)$ is shown as $s(\phi, t)$. The separation line lies on the nozzle wall and, in a nominally symmetric nozzle, the shock forms an azimuthally independent, average angle which varies with $x_s(t)$. Adapted from (Keanini et al., 2011).

(Keanini et al., 2011; Srivastava et al., 2010) - where fore and aft pressures, determined by the shock, differ significantly - a net, time- dependent side force, or *side load*, $\mathbf{F_s}$, is produced.

1.1 Connection to mass transfer

From a mass transfer perspective, a deep and unanticipated connection exists between the stochastic ascent of rockets subjected to side loading and damped diffusion processes. In order to understand the complex physical origins of this connection, it is necessary to first consider the purely mechanical features that connect shock-induced boundary layer separation to stochastic rocket response. Thus, much of this Chapter describes recent work focused on understanding these connections (Keanini et al., 2011; Srivastava et al., 2010). From a technological standpoint, the importance of separation-induced side loads derives from their sometimes catastrophic effect on rocket ascent. Side loads have been implicated, for example, in the in-flight break-up of rockets (Sekita et al., 2001), and in the failure of various rocket engine components (Keanini & Brown, 2007).

1.2 Chapter objectives

The objectives of this Chapter are as follows:

I) Two stochastic models (Keanini et al., 2011; Srivastava et al., 2010) and two simple (deterministic) scaling models (Keanini & Brown, 2007) have recently been proposed to describe shock-induced boundary layer separation within over-expanded rocket nozzles (Keanini & Brown, 2007; Keanini et al., 2011; Srivastava et al., 2010). Earlier work, carried out in the 1950's and 60's and focused on time-averaged separation behavior, lead to development of the Free Interaction model of boundary layer separation (Carriere et al., 1968; Chapman et al., 1958; Erdos & Pallone, 1962; Keanini & Brown, 2007; Ostlund, 2002). Our first objective centers on describing the physical bases underlying these models, as well as highlighting experimental evidence that supports the validity of each.

II) The stochastic boundary layer separation models developed in (Keanini et al., 2011; Srivastava et al., 2010) allow construction of stochastic side load models that, on one hand, are physically self-consistent, and on the other, are imbued with statistical properties that are fully consistent with available experimental observations. Our second objective focuses on describing these new stochastic side load models.

III) Given physically consistent separation and side load models (Keanini et al., 2011; Srivastava et al., 2010), the effect of random nozzle side loads on rocket ascent can be computed. Our group recently developed (Keanini et al., 2011) a series of interconnected, analytical models describing: i) fast time-scale, altitude-dependent stochastic boundary layer separation, ii) associated short-time- and long(rocket-dynamics)-time-scale stochastic side load generation, and iii) stochastic, altitude-dependent rocket response. In addition, a high-fidelity numerical model which solved the full nonlinear, coupled equations of rocket rotational and translational motion, under the action of altitude-dependent random side loads, was also reported (Srivastava et al., 2010). Our third objective centers on outlining these analytical and numerical models, and on describing recent results.

IV) Our most recent work (Keanini et al., 2011) demonstrates that rocket pitch and yaw rates evolve as Ornstein-Uhlenbeck processes. Since stochastic pitch and yaw rate evolution determines not only the random evolution of pitch/yaw displacement, but also the stochastic evolution of the rocket's lateral velocity and displacement (Keanini et al., 2011), the rocket's rotational and translational dynamics, fundamentally, trace to a damped diffusion process. The last objective centers on highlighting the connection between stochastic side load-driven rocket response and Ornstein-Uhlenbeck diffusion.

2. Boundary layer separation models and mean separation location

Two physically-based models of shock-induced separation were developed in 2007 (Keanini & Brown, 2007). The models assume importance for two reasons. First, they provide verifiable insight into the physical processes underlying shock-separation of compressible turbulent boundary layers. Second, they allow prediction of the altitude-dependent mean separation line, crucial in determining both the location and magnitude of altitude-dependent random side loads (Keanini et al., 2011; Srivastava et al., 2010). This section describes the more refined of these two models, as well as Chapman's Free Interaction Model (Chapman et al., 1958). All three models rely on scaling analyses of the boundary layer and near-boundary flows, in and near the boundary layer separation zone.

2.1 Time-average separation

Two distinct separation processes have been identified in overexpanded rocket nozzles, *free shock separation*, in which the turbulent boundary layer separates without reattachment, and *restricted shock separation*, in which the separated boundary layer reattaches, forming a small, closed recirculation zone immediately downstream of the separation point; see, e.g., (Keanini & Brown, 2007; Ostlund, 2002) for recent reviews of this work. This Chapter focuses on free shock separation.

The time-average flow features associated with free shock separation in nozzles were first characterized by Summerfield et al. (Summerfield et al., 1954), and are depicted schematically in figures 1 and 2. As shown, the time average pressure along the nozzle wall increases from P_i at the incipient separation point, x_i, to a peak value of P_p at x_p. Depending on the nozzle and the shock location relative to the nozzle exit, P_p is typically on the order of 80 to 100 % of the ambient pressure, P_a. The time-average separation point, x_s, lies immediately upstream of x_p.

Of central importance in nozzle design is determining both the conditions under which separation will occur and the approximate separation location. A number of criteria have been proposed for predicting the nominal free shock separation point, x_s; see, e.g., (Keanini & Brown, 2007; Ostlund, 2002) for reviews. Since the boundary layer pressure rise between x_i and x_s depends primarily on the inviscid flow Mach number, M_i, most criteria relate either a gross separation pressure ratio, P_i/P_a, or more recently, a refined ratio, P_i/P_p, to M_i (Ostlund, 2002). Given the separation pressure ratio, the separation location can then be determined using an appropriate model of flow upstream of separation.

Although the actual separation process is highly dynamic, the scaling model focuses on time average flow dynamics in the vicinity of the shock interaction zone. In order to provide physical context, we briefly review the dynamical features associated with free shock separation and note simplifying assumptions made. Shock motion over the shock interaction zone appears to be comprised of essentially two components: i) a low frequency, large scale motion produced by flow variations downstream of the separation point, and occurring over the length of the shock interaction zone, $l_p = x_p - x_i$, at characteristic frequencies, f_s [on the order of 300 to 2000 Hz in the case of compression ramp and backward facing step flows (Dolling & Brusniak, 1989)], and ii) a high frequency, low amplitude jitter produced by advection of vortical structures through the shock interaction zone (Dolling & Brusniak, 1989). The scaling models in (Keanini & Brown, 2007) limit attention to time scales that are long relative to f_s^{-1}. In addition, the model assumes that the flow is statistically stationary and that the separation process is two-dimensional.

The time average pressure gradient over the shock interaction zone ($x_i \leq x \leq x_p$), given approximately by

$$\frac{\partial P}{\partial x} \sim \frac{P_p - P_i}{l_p} \tag{1}$$

in reality reflects the intermittent, random motion of the shock between x_i and x_p; see, e.g., (Dolling & Brusniak, 1989). As the shock-compression wave system oscillates randomly above (and partially within) the boundary layer, the associated pressure jump across the system is transmitted across the boundary layer on a time scale $\tau_s \sim \delta_i/\sqrt{kRT_i}$, where δ_i and T_i are the characteristic boundary layer thickness and temperature in the vicinity of x_i. Under typical experimental conditions, τ_s is much shorter than the slow time scale, f_s^{-1} (where $\tau_s \approx$ 1 to $10\mu s$); thus, the instantaneous separation point essentially tracks the random position of the shock-compression wave system, where the position of the separation point is described by a Gaussian distribution over the length of the interaction zone (Dolling & Brusniak, 1989).

2.2 Scale analysis of shock-induced separation

In the vicinity of the separation point,x_s, we recognize that a fluid particle's normal acceleration component within the separating boundary layer is determined by the normal component of the pressure gradient across the separating boundary layer. Thus, balancing these terms (in the Navier- Stokes equations) yields:

$$\rho \frac{V_s^2}{R} \sim \frac{\partial P}{\partial n} \tag{2}$$

where V_s is the particle speed in the streamwise (s-)direction, and R^{-1} is the local streamline curvature. The curvature can be evaluated by first defining the shape of the boundary layer's

Constituent displacements in the set of N displacements are assumed independent, and based on experimental observations (Dolling & Brusniak, 1989), gaussian. Thus, each p_I is given by

$$p_I(s_I) = \frac{1}{\sqrt{2\pi\sigma_s^2}} \exp\left[-\frac{s_I^2}{2\sigma_s^2}\right] \tag{22}$$

In moving to a continuous description of the separation line, (Srivastava et al., 2010) assumes that

$$< s(\phi, t)s(\phi', t) >= \sigma_s^2 \delta(\phi - \phi') \tag{23}$$

Considering next the side load, we express the instantaneous force vector produced by

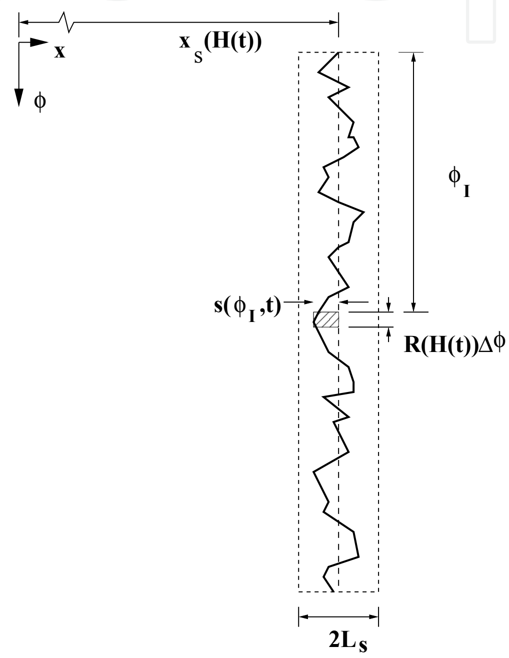

Fig. 7. Model I (Srivastava et al., 2010) separation line model. The mean separation line position, $x_s(H(t))$, moves down the nozzle axis, on the slow time scale associated with vertical rocket motion. By contrast, axial separation line motion about $x_s(H(t))$, at any angular position, ϕ_I, is random, and takes place on a much shorter time scale. Rapid axial motion, in addition, is confined to the nominal shock-boundary layer interaction zone, again denoted by L_s. Pressures upstream and downstream of the instantaneous separation line, $P_i = P_i(H(t))$ and $P_2 = P_2(H(t))$, respectively, are assumed to be spatially uniform within L_s. Adapted from (Srivastava et al., 2010).

asymmetric boundary layer separation, $\mathbf{F_s}(t)$, as a sum of radial and axial components

$$\mathbf{F_s}(t) = \mathbf{F_r}(t) + \mathbf{F_x}(t) \tag{24}$$

In (Srivastava et al., 2010), the following *ad hoc* side load model was assumed:

A) F_{sy} and F_{sz} are independent, gaussian random variables,

B) $< F_{sy} >= 0$ and $< F_{sz} >= 0$,

C) $\left\langle \left(F_{sy}- < F_{sy} > \right)^2 \right\rangle = \left\langle \left(F_{sz}- < F_{sz} > \right)^2 \right\rangle = \sigma^2$, where, assuming ergodicity, $< \cdot >$ denotes either an ensemble or time average, and where the separation line model above is used to calculate the force variance σ^2. The side load components F_{sy} and F_{sz} are expressed with respect to rocket-fixed coordinates; see (Keanini et al., 2011; Srivastava et al., 2010).

In order to demonstrate the physical consistency of the model introduced in (Srivastava et al., 2010), (Keanini et al., 2011) first shows that the *assumed* properties, A) -C), can be *derived* from the simple *separation line model* developed in (Srivastava et al., 2010). Second, and as shown in the next subsection, the side load model in A) - C) then leads to *experimentally observed* side load amplitude and direction densities (Keanini et al., 2011).

3.1 Derivation of density functions for side load amplitude and direction

Two important experimental and numerical observations concerning the side load, $\mathbf{F_s}$ (within rigid, axisymmetric nozzles) are first noted:

a) the probability density of the random amplitude, $A = |\mathbf{F_s}|$, is a Rayleigh distribution (Deck & Nguyen, 2004; Deck et al., 2002), and

b) the random instantaneous direction, ϕ_s, of $\mathbf{F_s}$ is uniformly distributed over the periphery of the nozzle, or $p_{\phi_s}(\phi_s) = 1/2\pi$, where p_{ϕ_s} is the pdf of the side load direction (Deck & Nguyen, 2004; Deck et al., 2002).

Both observations can be *derived*, starting from the simple statistical model of random side loads, A) - C), immediately above. Thus, given A and ϕ_s, the instantaneous side load components in body-fixed y and z directions are given by

$$F_{sy} = A\cos\phi_s \qquad\qquad F_{sz} = A\sin\phi_s$$

Following (Srivastava et al., 2010), write F_{sy} and F_{sz} as $F_{sy} = \bar{Y} = A\cos\phi_s$ and $F_{sz} = \bar{Z} = A\sin\phi_s$; thus, the joint probability density associated with F_{sy} and F_{sz} can be expressed as

$$p_{\bar{Y}\bar{Z}}(\bar{Y},\bar{Z}) = p_{\bar{Y}}(\bar{Y})p_{\bar{Z}}(\bar{Z}) = \frac{1}{2\pi\sigma^2}\exp\left(-\frac{\bar{Y}^2+\bar{Z}^2}{2\sigma^2}\right) \tag{25}$$

Following (Srivastava et al., 2010), we restate $p_{\bar{Y}\bar{Z}}$ in terms of A and ϕ_s as,

$$p_{A\phi_s} = |J|p_{\bar{Y}\bar{Z}}(\bar{Y},\bar{Z}) \tag{26}$$

where $p_{A\phi_s}(A,\phi_s)$ is the joint pdf for the random amplitude and direction of $\mathbf{F_r}$, and where the jacobian determinant is given by

$$|J| = \begin{vmatrix} \frac{\partial\bar{Y}}{\partial A} & \frac{\partial\bar{Y}}{\partial\phi_s} \\ \frac{\partial\bar{Z}}{\partial A} & \frac{\partial\bar{Z}}{\partial\phi_s} \end{vmatrix} = A \tag{27}$$

Thus,

$$p_{A\phi_s}(A,\phi_s) = \frac{A}{2\pi\sigma^2}\exp\left(-\frac{A^2}{2\sigma^2}\right) = \left(\frac{1}{2\pi}\right)\left[\frac{A}{\sigma^2}\exp\left(-\frac{A^2}{2\sigma^2}\right)\right] = p_{\phi_s}(\phi_s)p_A(A) \tag{28}$$

where,

$$p_{\phi_s}(\phi_s) = \frac{1}{2\pi} \qquad\qquad 0 < \phi_s \leq 2\pi \tag{29}$$

is the uniform probability density underlying the random direction ϕ_s, and

$$p_A(A) = \frac{A}{\sigma^2} \exp\left(-\frac{A^2}{2\sigma^2}\right) \tag{30}$$

is the Rayleigh distribution for the amplitude A.

3.2 Ornstein-Uhlenbeck model of separation line dynamics

Theoretical determination of rocket response to side loads requires that the time correlation function for either side load component, $\langle F_{s\alpha}(t')F_{s\alpha}(t)\rangle$, be first determined. As detailed in (Keanini et al., 2011), $\langle F_{s\alpha}(t')F_{s\alpha}(t)\rangle$ is developed in two steps. First, and as detailed in this subsection, we propose(and physically justify) that local separation line dynamics can be modeled as an Ornstein-Uhlenbeck process. Once this assumption is made, then the second step rests on a rigorous argument showing that on the relatively long rocket dynamics time scale, the boundary layer separation line shape, and importantly, associated side load components, are all delta correlated in time. See (Keanini et al., 2011)for details.

The following simple, explicit stochastic model of separation line dynamics is proposed:

$$ds_i(t) = -ks_i(t) + \sqrt{D_s}dW(t) \tag{31}$$

where $s_i(t) = s(\phi_i, t)$ is the instantaneous separation line position at ϕ_i, k and D_s are damping and effective diffusion coefficients, and $dW(t)$ is a differential Weiner process. This equation, describing an Ornstein-Uhlenbeck process, allows straightforward, physically consistent calculation of statistical properties associated with separation line motion and, more importantly, serves as the first link in a chain that connects short-time-scale random separation line motion to short-time-scale random side loads, and in turn, to long-time-scale stochastic rotational rocket dynamics (Keanini et al., 2011).

The form of this equation is chosen based on the following experimental features, observed in shock-separated flows near compression corners and blunt fins:

a) Under statistically stationary conditions, the feet of separation-inducing shocks oscillate randomly, up- and downstream, over limited distances, about a fixed mean position; see, e.g., (Dolling & Brusniak, 1989).

b) As observed in (Dolling & Brusniak, 1989)the distribution of shock foot positions within the shock-boundary layer interaction zone is approximately gaussian.

c) The time correlation of shock foot positions, as indicated by wall pressure measurements within the shock-boundary layer interaction zone, decays rapidly for time intervals, $\triangle t$, larger than a short correlation time, τ_s, a feature that can be inferred, for example, from (Plotkin, 1975).

Physically, the damping term captures the fact that the shock sits within a pressure-potential energy well. Thus, downstream shock excursions incrementally decrease and increase, respectively, upstream and downstream shock face pressures; the resulting pressure imbalance forces the shock back upstream. A similar mechanism operates during upstream excursions. Introduction of a Weiner process models the combined random forcing produced by advection of turbulent boundary layer structures through the upstream side of the shock foot and pressure oscillations emanating from the downstream separated boundary layer and recirculation zone.

We note that the proposed model is qualitatively consistent with Plotkin's model of boundary layer-driven shock motion near compression corners and blunt fins (Plotkin, 1975). Plotkin's model, which captures low frequency spectra of wall pressure fluctuations within these flows, corresponds to a generalized Ornstein-Uhlenbeck process in which a deterministic linear damping term is superposed with a non-Markovian random forcing term. We use an ordinary OU process model, incorporating a Weiner process, since again, it is consistent with the above observations and more particularly, since it allows much simpler calculation of statistical properties (Keanini et al., 2011).

4. Rocket response to random side loads

This section highlights recent results on numerical simulation of the stochastic ascent of a sounding-rocket-scale rocket, subjected to altitude dependent random nozzle side loads (Srivastava et al., 2010). The numerical simulations solve the full, coupled, nonlinear equations of rotational and translational rocket motion. The simulations include the effects of altitude-dependent aerodynamic drag forces, random nozzle side loads, associated random torques, mass flux damping torques (Keanini et al., 2011), and time-varying changes in rocket mass and longitudinal moment of inertia. In order to clearly isolate the effects of nozzle side loads on rocket translational and rotational dynamics, random wind loads are suppressed. A simple scaling argument (Keanini et al., 2011) indicates that random winds: i) under most conditions, do not excite rotational motion, and ii) simply function as an *additive* source of variance in the rocket's *translational* motion. In other words, wind appears to have minimal influence on the stochastic, altitude-dependent evolution of *rotational* dynamics. Rather, (launch-site-specific) mean and random winds simply produce whole-rocket, random, *lateral translational* motion, superposed on a deterministic translational drift.

Given side load direction and amplitude densities in Eqs. (29) and (30), respectively, altitude- dependent side loads are simulated using a Monte Carlo approach; the nonlinear, coupled equations of translational and rotational motion are then solved using fourth order Runge-Kutta integration (Srivastava et al., 2010). In estimating altitude-dependent means and variances in translational and rotational velocities and displacements, an ensemble of 100 simulated flights are used; it is found that estimated statistics do not vary significantly when using ensembles of 40 and 100 flights (Srivastava et al., 2010). The parameters employed in the simulations are characteristic of medium sized sounding rockets (Srivastava et al., 2010).

Characteristic results are presented in figures 8 through 13. The stochastic evolution of both lateral side load components, F_{sy} and F_{sz}, observed during a single simulated realization, is shown in figure 8. Initially, i.e., at launch, the pressure jump across the separation-inducing shock is relatively high (Srivastava et al., 2010), and is manifested by somewhat higher initial side load amplitudes. However, as the rocket gains altitude, ambient pressure decays, and the cross-shock pressure jump decreases - characteristic side load magnitudes become smaller. At the instant when the slowly traveling in-nozzle shock reaches the nozzle exit, the nozzle flow becomes shock free, boundary layer separation ceases, and side loading stops. For these simulations, this instant corresponds to a flight time of 10.85 seconds (Srivastava et al., 2010), or an altitude of approximately 3.75 km. Note that side load amplitudes are significant, on the order of 10 to 16 % of the rocket's initial weight.

Figure 9 shows a single realization of the rocket's trajectory, under the action of random side loads, and is compared against the trajectory taken when side loads are suppressed. [Here, and throughout, X_o and (Y_o, Z_o) denote, respectively, the vertical, and (mutually orthogonal) lateral displacements of the rocket center of mass, relative to the launch location.] It is clear, that absent active control, a rocket can exhibit significant lateral displacements relative to the predicted zero-side-load path. Scaling shows that the characteristic magnitudes of random

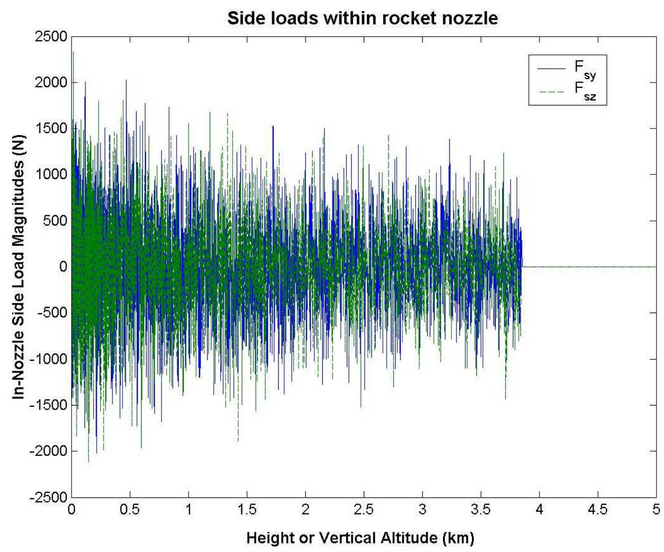

Fig. 8. In-nozzle stochastic side loads versus rocket altitude. Adapted from (Srivastava et al., 2010).

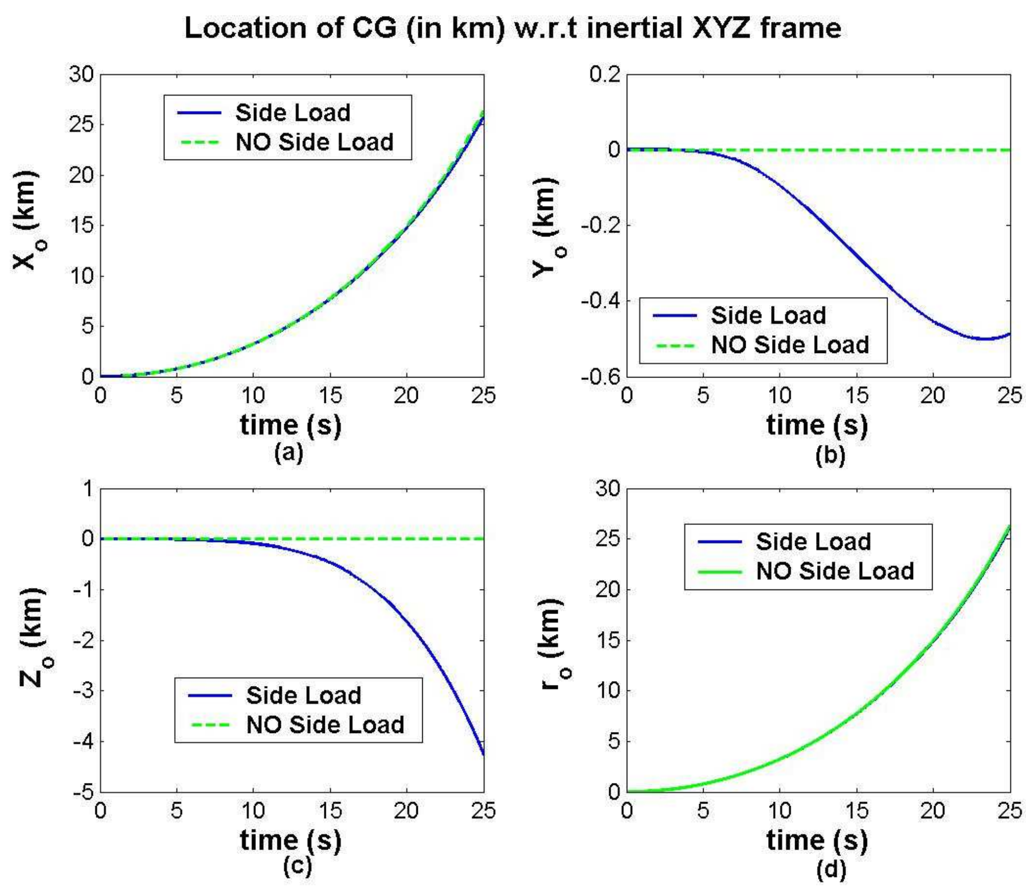

Fig. 9. Single realizations of rocket center of mass trajectory under random side loads and with side loads suppressed. X_o, and (Y_o, Z_o) denote, respectively, the vertical, and (mutually orthogonal) lateral displacements of the rocket center of mass, relative to the launch location. Adapted from (Srivastava et al., 2010).

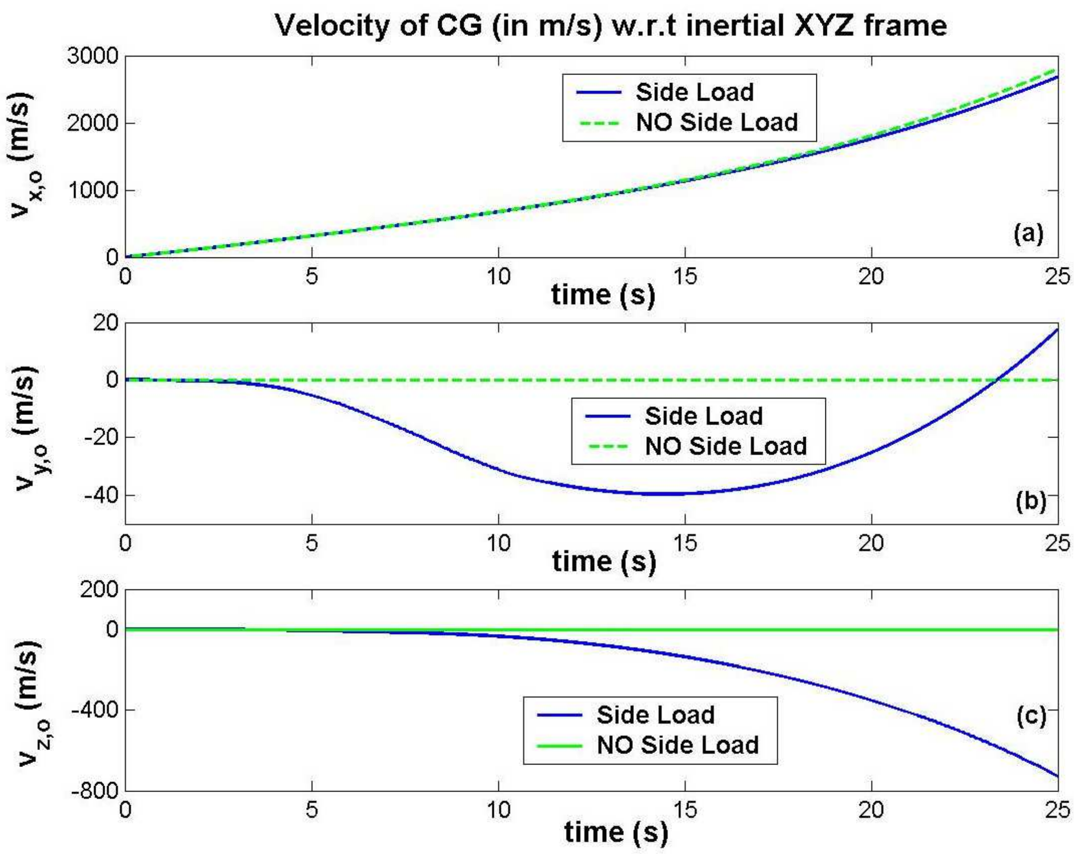

Fig. 10. Single realizations of rocket center of mass velocity under random side loads and with side loads suppressed. $v_{x,o}$ and $(v_{y,o}, v_{z,o})$, denote, respectively, the vertical, and (mutually orthogonal) lateral velocities of the rocket center of mass, relative to the launch location. Adapted from (Srivastava et al., 2010).

lateral displacements, which can be on the order of 1-4 kilometers over the simulated flight time of 25 seconds, are fully consistent with displacements estimated using characteristic side load magnitudes (Keanini et al., 2011; Srivastava et al., 2010). The several order of magnitude difference between (vertical) thrust forces and the small vertical component of $\mathbf{F_s}$ explains the result shown in figure 8a.

Random side loads produce significant excitation of pitch and yaw dynamics (Keanini et al., 2011; Srivastava et al., 2010). Thus, for example, once a rocket begins a random pitching and yawing motion, that motion continues, even after side loading stops (at $t = 10.85$ s). Random pitch and yaw, in turn, produce random lateral velocities. As indicated in figures 10 and 11, and as discussed in detail in (Keanini et al., 2011), a certain amount of time - an induction period - must pass before side-load-induced pitch and yaws grow large enough for significant lateral thrust components to appear. Once the induction period has passed, however, large lateral thrusts begin to act and the rocket begins to experience large lateral velocities and displacements. Figures 10 and 11 capture these essential dynamical features. The work in (Keanini et al., 2011) provides a detailed, physically-based analysis of the complex dynamics a rocket experiences during side loading.

As shown in (Keanini et al., 2011), and as indicated in figure 12, stochastic pitch and yaw rotational dynamics are characterized by two qualitatively distinct regimes. During the side load period, $t \leq 10.85$ s, the action of random side loads on pitch and yaw angular velocities

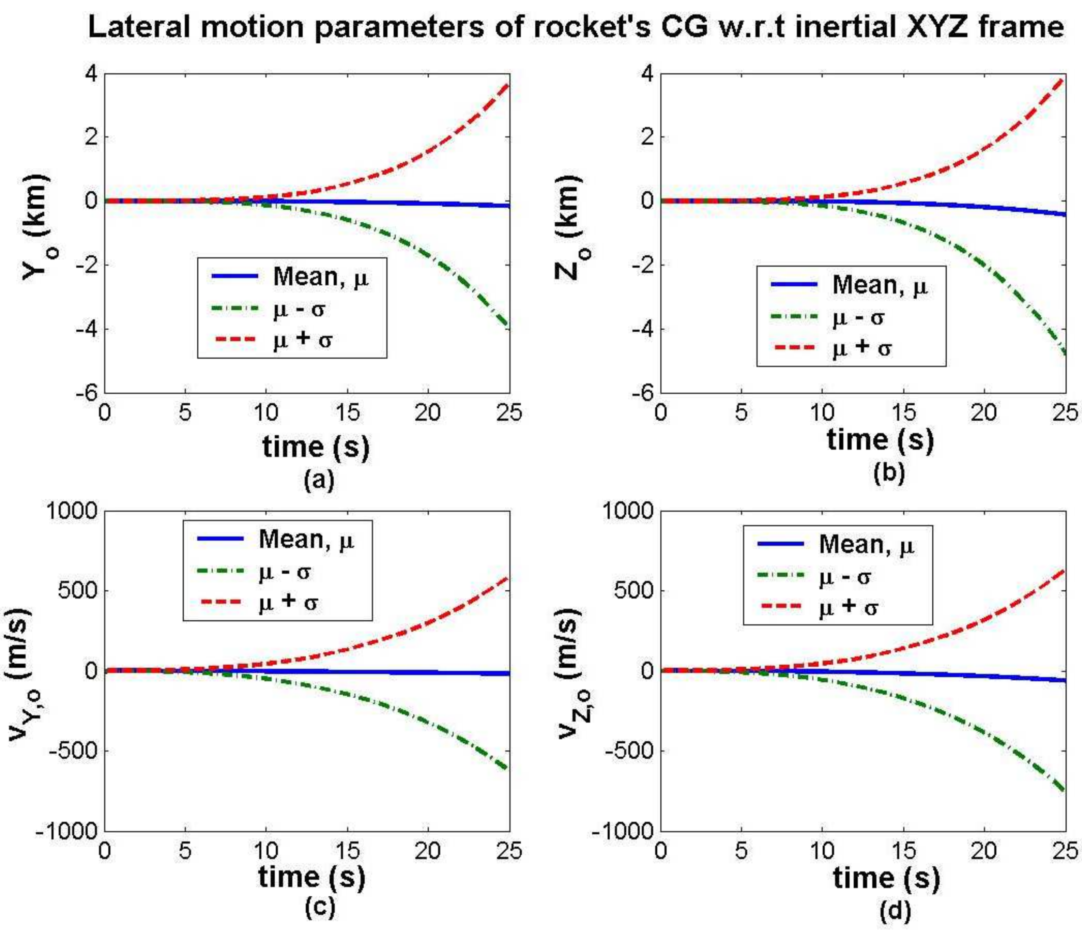

Fig. 11. Time-(altitude-)dependent means and variances of the rocket's lateral center of mass position (Y_o, Z_o) and lateral center of mass velocity (v_{yo}, v_{zo}). Adapted from (Srivastava et al., 2010).

can be modeled as an Ornstein-Uhlenbeck process, wherein side loads function, at least on the long rocket dynamics time scale, as Weiner processes. Simultaneous to stochastic pitch/yaw amplification, deterministic pitch/yaw damping, produced by incremental changes in the nozzle mass flux vector, i.e., mass flux damping (Keanini et al., 2011), counteract amplification. Thus, during the side load period, pitch/yaw velocities grow, but at an ever-decreasing rate. In the second regime, which begins when the separation-inducing shock exits the nozzle and side loads cease, mass-flux damping continues, driving pitch and yaw velocities toward zero (Keanini et al., 2011). These qualitative features are likewise apparent in plots of time-(altitude-)dependent pitch/yaw means and variances; see figure 13. As detailed in (Keanini et al., 2011), all of these features can be rigorously explained using, e.g., a course grained description of short-time-scale side load statistics, along with an asymptotic model of rocket translational and rotational motion.

5. Stochastic rocket ascent as a diffusion process

Starting with the nonlinear equations of rotational motion, (Keanini et al., 2011) use a rigorous argument to show that the equations governing evolution of pitch and yaw rates assume the

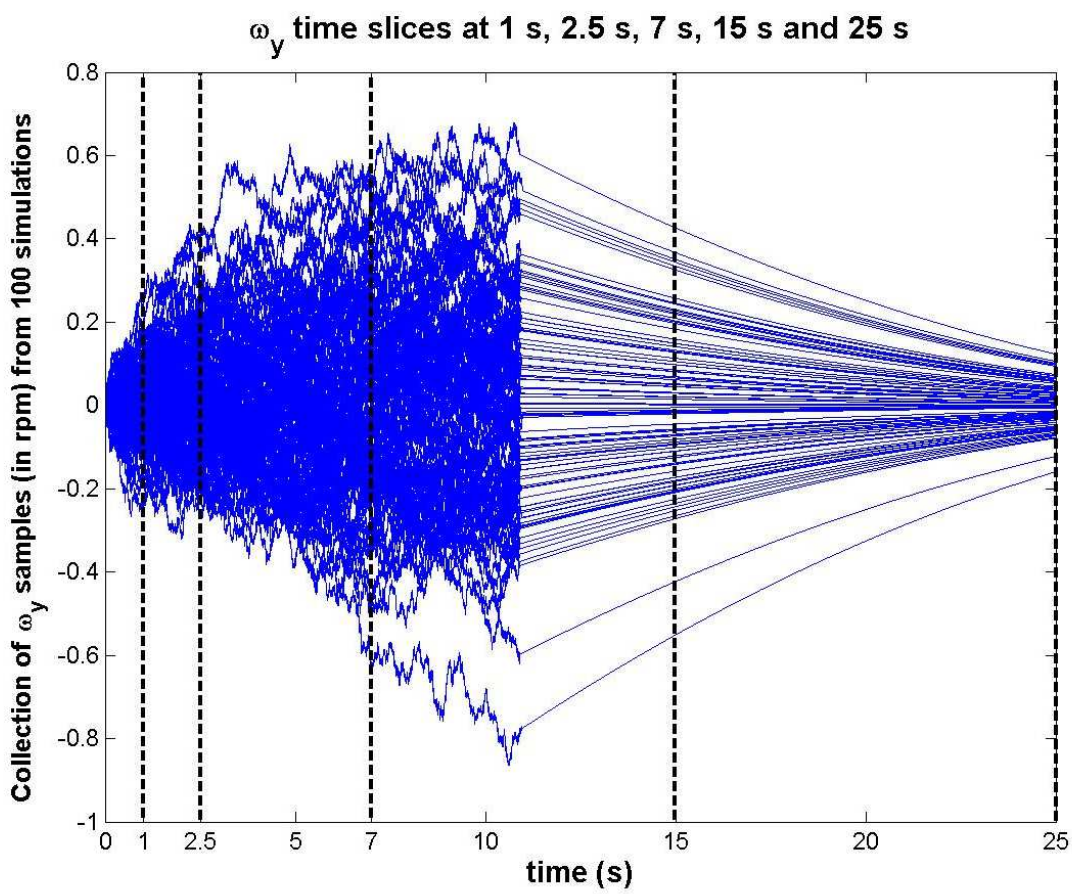

Fig. 12. Ensemble of 100 realizations of yaw angular velocity evolution. Side loads cease at $t = 10.85$ s. Adapted from (Srivastava et al., 2010).

form of an Ornstein-Uhlenbeck process:

$$d\omega_{\pm} = -A(t)\omega_{\pm} \pm \sqrt{D(t)}dW_{\pm} \quad (32)$$

where $\omega_+ = \omega_y$ and $\omega_- = \omega_z$ correspond, respectively, to yaw and pitch rate, $A(t)$ and $D(t)$ are, respectively, the time-(altitude-)dependent effective damping and diffusion coefficients, and $W_{\pm}(t)$ are Weiner processes.

Fundamentally, and as detailed in (Keanini et al., 2011), equation (32) provides the key to analyzing both the rotational and translational rocket response to side loading. Physically, $A(t)$ is roughly proportional to both the squared moment arm from the rocket center of mass to the nozzle exit, L_{ce}^2, as well as the mass flux magnitude, and is inversely proportional to the lateral moment of inertia. Likewise, $D(t)$ is proportional L_{ce}^2, as well as the squared (altitude-dependent) pressure difference between the interior and exterior of the nozzle, and the squared altitude-dependent position of the separation-inducing shock.

Practically, the detailed formulas for $A(t)$ and $D(t)$ in (Keanini et al., 2011) are related to both rocket-specific design parameters, as well as universal, non-specific parameters characterizing in-nozzle, shock-boundary layer separation. Thus, as discussed in (Keanini et al., 2011), the formulas allow straightforward identification of design criteria for, e.g., enhancing pitch/yaw damping and/or suppressing diffusive, i.e., stochastic growth of random pitch and yaw.

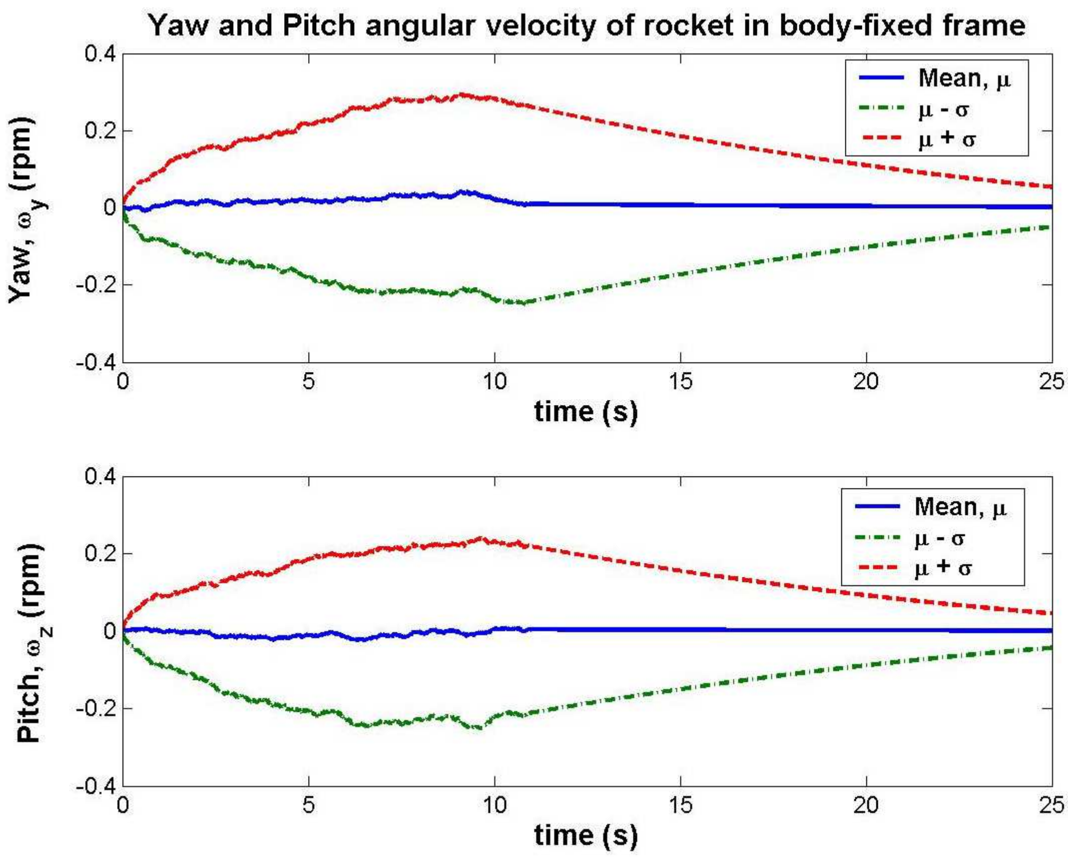

Fig. 13. Time-(altitude-)dependent means and variances of the rocket's pitch and yaw angular velocities. Adapted from (Srivastava et al., 2010).

6. References

Bloomer, H. E., Antl, R. J. & Renas, P. E. (1961). Experimental study of the effects of geometric variables on performance of conical rocket engine exhaust nozzles, NASA TN D-846.

Carriere, P., Sirieix, M. & Solignac, J. L. (1968). Properties de similitude des phenomenes de decollement laminaires ou turbulents en ecoulement supersonic nonuniforme, *12th Int. Congress of Applied Mech.*, Stanford Univ., Palo Alto, CA.

Chapman, D. R., Kuehn, H. K. & Larson, H. K. (1958). Investigation of separated flows in supersonic and subsonic streams with emphasis on the effect of transition, NACA Report 1356.

Deck, S. & Nguyen, A. T. (2004). Unsteady side loads in thrust-optimized contour nozzle at hysteresis regime, *AIAA J.*, Vol. 42, No. 9, pp. 1878-1888.

Deck, S., Garnier, E. & Guillen, P. (2002). Turbulence modeling applied to space launcher configurations, *J. Turbulence*, Vol. 3, No. 1, pp. 57-57(1).

Dolling, D. S. & Brusniak, L. (1989). Separation shock motion in fin, cylinder, and compression ramp-induced turbulent interactions, *AIAA J.*, Vol 27, No. 6, pp. 734-742.

Erdos, J. & Pallone, A. (1962). Shock-boundary layer interaction and flow separation, *Proc Heat Transfer and Fluid Mechanics Institute*, Stanford Univ. Press.

Flemming, E. L., Chandra, S., Schoeberl, M. R. & Barnett, J. J. (1988). Monthly Mean Global Climatology of Temperature, Wind, Geopotential Height, and Pressure for 0-120 km, NASA TM-100697.

Frey, M. & Hagemann, G. (1998). Status of flow separation prediction in rocket nozzles, AIAA Paper 98-3619.

Gruntman, M. (2004). *Blazing The Trail: The Early History Of Spacecraft and Rocketry,* AIAA, Reston, VA.

Justus, C. G. & Johnson, D. L. (1999). The NASA/MSFC Global Reference Atmospheric Model -1999 Version, NASA TM-1999-209630.

Justus, C. G., Campbell, C. W., Doubleday, M. J. & Johnson, D. L. (1990). New Atmospheric Turbulence Model for Shuttle Applications, NASA TM-4168.

Keanini, R. G. & Brown, A. (2007). Scale analysis and experimental observations of shock-induced turbulent boundary layer separation in nozzles, *European J. Mechanics B/Fluids,* Vol. 26, pp. 494-510.

Keanini, R. G., Srivastava, N. & Tkacik, P. T. (2011). Stochastic rocket dynamics under random nozzle side loads: Ornstein-Uhlenbeck boundary layer separation and its course grained connection to side loading and rocket response, in press *Annalen der Physik.*

Leahy, F. B. (2008). Discrete gust model for launch vehicle assessements, 12^{th} *Conf. on Aviation, Range and Aerospace Metrology,* Atlanta, GA, Jan. 2006, American Meteorology Society..

McNaughtan, I. I. (1993). The resistance of transparencies to bird impact at high speeds, *Aircraft Engrg. Aerospace Tech.,* Vol. 36, No. 12, pp. 409-413.

Ostlund, J. (2002). Supersonic flow separation with application to rocket engine nozzles, Doctoral Thesis, Department of Mechanics, Royal Institute of Technology, Stockholm, Sweden.

Plotkin, K. J. (1975). Shock wave oscillation driven by turbulent boundary-layer fluctuations, *AIAA J.,* Vol. 13, No. 8, pp. 1036-1040.

Schmucker, R. H. (1984). Flow Processes in Overexpanded Chemical Rocket Nozzles - Part I, NASA Rep. 77396.

Sekita, R., Watanabe, A., Hirata, K. & Imoto, T. (2001). Lessons learned from H-2 failure and enhancement of H-2A project, *Acta Astronautica,* Vol. 48, No. 5-12, pp. 431-438.

Srivastava, N., Tkacik, P. T. & Keanini, R. G. (2010). Influence of nozzle random side loads on launch vehicle dynamics, *J. Applied Physics,* Vol. 108, pp. 044911-044926.

Summerfield, M., Foster, C. R. & Swan, W. C. (1954). Flow separation in overexpanded supersonic exhaaust nozzles, *Jet Propulsion,* Vol. 24, No. 9, pp. 319-321.

Sutton, G. P. & Biblarz, O. (2001). *Rocket Propulsion Elements, 7th ed,* Wiley, New York.

Mass Transfer - Advanced Aspects

Edited by Dr. Hironori Nakajima

ISBN 978-953-307-636-2
Hard cover, 824 pages
Publisher InTech
Published online 07, July, 2011
Published in print edition July, 2011